Heliyon 10 (2024) e25629

Contents lists available at ScienceDirect

Heliyon

journal homepage: www.cell.com/heliyon

Research article

Innovatively feasible wet incipient method for preparing Cu doped TiO_2 nanocomposite: Electro-optical measurement supported by quantitative quantum and classical calculations

Ali H. Bashal [a,*], Hana Al-Refai [a], R.M. Ibrahim [b], Ayman A. Zaki [c,d]

[a] Department of Chemistry, Faculty of Science, Taibah University, Yanbu, 46423, Saudi Arabia
[b] Department of Physics, Faculty of Science, Taibah University, Al-Madinah, 46423, Saudi Arabia
[c] Department of Physics, Faculty of Science, Taibah University, Yanbu, 46423, Saudi Arabia
[d] Department of Physics, Faculty of Science, Benha University, Egypt

ARTICLE INFO

Keywords:
Cu/TiO_2
Dialectical properties
Optical properties
Quantum calculations
Classical calculations

ABSTRACT

The Cu-doped titanium oxide (Cu/TiO_2) nanocomposite was systematically prepared using the innovatively feasible incipient wet impregnation method. Notably, the samples were derived from the raw materials through water dilution only. The successful formation of the host anatase TiO_2 phase was confirmed by the characteristic peaks observed in the acquired X-ray powder diffraction (XRD) spectrum, which displayed intense peaks attributed to Cu^{2+} scattering sites, indicating the formation of crystallite Cu/TiO_2 nanostructures. Dielectric measurements revealed that Cu/TiO_2 possesses a higher dielectric permittivity compared to undoped TiO_2. The conductivity for both structures exhibited a decreasing trend with increasing temperature. Interestingly, the measured optical properties indicated that Cu/TiO_2 exhibited the minimum energy gap and maximum refractive index. This was further validated by qualitative time-dependent density functional calculation on a stable structural model, which was confirmed through semi-empirical molecular dynamic calculations. Thus, we have demonstrated the capability of our innovatively feasible synthesis method to produce the industrially important Cu-doped TiO_2.

1. Introduction

In contemporary times, there is a notable focus on electrochemical capacitors as a means of energy storage. This emphasis is primarily driven by their rapid charge and discharge properties, substantial power density, cost-effectiveness, extended lifespan, and eco-friendly nature [1,2]. A diverse range of oxide semiconductors, such as TiO_2, MnO_2, NiO, MoO_3, Co_3O_4, among others, is commonly employed as electrode materials in the context of supercapacitor applications [3]. It is widely acknowledged that titanium dioxide possesses exceptional dielectric properties and exhibits cost-effective faradaic charge storage behavior [4,5]. However, the utilization of TiO_2 as a standalone electrode material for supercapacitors yields comparatively subpar performance [6]. Therefore, combining TiO_2 with various metals or nonmetals (e.g., Cu [7], Ni [8], Mn [9], Co [10]) leads to a decrease in bandgap energy, improvement in optical response, and an increase in charge carrier concentration. These collective effects contribute to the

* Corresponding author.
E-mail addresses: abishil@taibahu.edu.sa (A.H. Bashal), hhjuhani@taibahu.edu.sa (H. Al-Refai), rtum@taibahu.edu.sa (R.M. Ibrahim), ayman_a73@hotmail.com (A.A. Zaki).

https://doi.org/10.1016/j.heliyon.2024.e25629
Received 25 November 2023; Received in revised form 30 January 2024; Accepted 31 January 2024
Available online 6 February 2024

improvement of super-capacitive characteristics and power conversion efficiency in the novel system [11,12]. Krishnan et al. [13] conducted a study whereby they observed that the use of nickel as a dopant in titanium dioxide nanofibers resulted in enhanced conductivity and improved specific capacitance. Specifically, they noted an increase in specific capacitance from 40 to 179 F g^{-1} at a current density of 1 A g^{-1}. An enhanced specific capacitance was observed by a separate research group subsequent to the introduction of a 2 % Ta dopant into titanium dioxide. The researchers discovered that the specific capacity of 2 % Ta-doped titanium dioxide nanofibers was measured to be 199 F g^{-1}, whereas pure TiO_2 exhibited a specific capacity of 111 F g^{-1} under the same experimental conditions of a scan rate of 5 mV/s in a 1 M sulfuric acid electrolyte. Furthermore, these materials have demonstrated exceptional cycle stability, with a retention rate of around 100 % in specific capacity after undergoing 3000 cycles [14]. Conversely, the impact of doping on the participation of charge carriers in the electrical conduction of semiconductors might be significant [15]. Copper has been widely employed by numerous researchers as a dopant to manipulate the optical and dielectric properties of TiO_2. Nevertheless, the synthesis methodology employed in these studies is intricate and sometimes time-consuming [15,16]. Hence, our research was driven by the motivation to concentrate on the efficient synthesis of Cu/TiO_2 through a simple incipient wet impregnation technique, eliminating the requirement for surfactants.

Two things make this work advantageous: first, we show that our simple and practical synthesis method works, and second, the resulting Cu/TiO_2 has various optical and electrical applications [17]. These applications include, but are not limited to, super-capacitors and composites for effective dye-sensitized solar cells [18–20]. Since, novel catalytic activities can be achieved via the systematic doping of TiO_2 with various metals as reported, for instance, by Shu et al. who demonstrated the novel photocatalyst activity of the Cu-Cu_xO/TiO_2 composite [21].

The synthesized material in our work, Cu/TiO_2, was subjected to X-ray diffraction examination to clarify its main properties and potential uses. Additionally, the dielectric, conductivity, and optical characteristics of Cu/TiO_2 and TiO_2 nanostructures were studied. Consequently, the goal of this work was to create a thorough framework for comprehending how Cu doping affects the chemical and physical characteristics of the resultant nanocomposite. Furthermore, semi-empirical molecular dynamic calculations were used to qualitatively confirm the structural stability of Cu/TiO_2. To sum up, the study showed that Cu/TiO_2 samples that were synthesized in a novel and simple way have a wide range of applications and a great deal of promise for use as high-performance dielectrics and pseudocapacitors [22].

2. Experimental

2.1. Materials

Copper chloride and titanium oxide, both of which were purchased from Sigma-Aldrich (USA) with high purity (≥99 % metallic trace basis), were used as starting ingredients to synthesize the metal oxide particles. The aqueous solutions required for the composite synthesis using the straightforward incipient wet impregnation approach were made using deionized water. Every chemical that was used in the synthesis process was used in the exact purity that the supplier had provided.

2.2. Sample preparation

We strictly adhere to the protocol described in our earlier work [23], which is depicted in Fig. 1 below. This protocol just used the incipient wet impregnation approach to prepare the Cu/TiO_2. In this approach, the mixture had to be constantly stirred for around 30 min in order to achieve the dispersion of undoped TiO_2 in water (1 g: 5 ml).

One weight percent (wt. %) of $CuCl_2$ was dissolved in 3 ml of deionized water and introduced to prepared mixture. To ensure the formation of a homogeneous mixture, the prepared $CuCl_2$ solution was gradually added to the TiO_2 solution. The resultant mixture was dried in a drier set at 120 °C for 12 h. The dried samples with a 1 wt percent Cu content will be referred to as Cu/TiO_2. In order to form a pellet that was used for material measurements and dielectric characterizations, about 0.30g of the finely ground powder from the samples was carefully compressed in a hydraulic press.

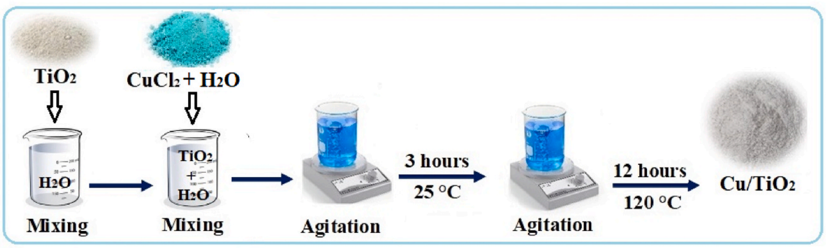

Fig. 1. Preparation of Cu/TiO_2 nanoparticle.

2.3. Sample characterization

The atomic phase structure of the samples was examined using XRD (X-ray Diffraction). The X-rays were generated by bombarding a Cu target with an electron beam energized by a 40 kV power supply (at 30 mA) to produce Kα radiation with a wavelength (λ) of 0.15418 nm. The temperature dependence of the samples' dielectric properties was determined using the "Solareton Analytic" impedance analyzer with a frequency-dependent excitation signal and a 300 mV signal amplitude.

3. Results and discussion

3.1. Characterizations of Cu-doped TiO_2

3.1.1. XRD

XRD patterns for TiO_2 and Cu/TiO_2 are shown in Fig. 2. The curved parenthesis adjacent to "R" and "A" denotes the appropriate Miller plane indices.

The rutile and anatase phases are represented by the peaks labeled "R" and "A," respectively. The undoped TiO_2 diffraction peaks at $2\theta^o = 25.3°$, 37.69°, 48.03°, 53.83°, 55.01°, 62.8°, 68.8°, 70.4°, 75.2°, and 76° are accredited to the A101, A004, A200, A105, A211, A204, A116, A220, A215, and A301 diffraction planes. According to Wang et al. [24], these planes are part of the tetragonal phase for the anatase phase. However, for the Cu-doped sample, the XRD revealed no specific peaks relevant to the Cu dopants. This could possibly arise from the low metallic (Cu) percentage in the analyzed sample, or it is possible that the Cu doping level may not be resolved by the XRD. In addition, we observed no significant shift (due to doping effects) towards high diffraction angles in the XRD peaks for the Cu/TiO_2, indicating that the copper ion's size is significantly greater than Ti4+, allowing copper to bind to the surface of TiO_2 crystallites. This adsorption is governed by the surface interaction. Furthermore, the incorporation of Cu^{2+} into the TiO_2 structure makes the XRD peaks for Cu/TiO_2 quite intense, which may indicate the formation of a fine crystalline structure of the prepared Cu/TiO_2, in agreement with the literature [25].

3.1.2. SEM/EDS analysis

The structures of undoped TiO_2 and Cu-doped TiO_2 are shown in Fig. 3 using SEM images.

Comparing the images in Fig. 3 will indicate significant distinctions between the microstructures, such as the smaller average size for the TiO_2 granular structure compared to that for Cu/TiO_2. Overall, the aggregation of smaller particles of Cu/TiO_2 may have led to the formation of the observed semispherical granular structures seen in Fig. 3(b). The confirmation of dopant existence is given by the EDS spectrum of Cu-doped TiO_2 (Fig. 3(c)). Fig. 3(c) depicts the Cu/TiO_2 sample's EDS elemental analysis, which was achieved in the area revealed by the SEM in Fig. 3(b). Ti and O, the primary components of Cu/TiO_2, display substantial X-ray peaks on the chemical composition graph in Fig. 2, indicating that Cu is likely distributed uniformly throughout TiO_2. It is possible that in this situation, Ti and O ratios are connected to the typical 1:2 stoichiometry. The proportional weight of Cu in TiO_2 and the highest EDS intensity coincide, indicating that TiO_2 has been efficiently doped with Cu.

3.2. Molecular dynamic calculation for rough assessment of the stability of Cu nanoparticle on TiO_2 support

We performed molecular dynamic calculations based on the semi-empirical quantum tight-binding method to roughly assess the geometrical stability of a Cu nanoparticle (for simplicity, 6 Cu atoms cluster was used) on a TiO_2 support. The MD time was 100 ps, resulting in the Cu/TiO_2 structure shown in Fig. 4. To approximately emulate the bulk TiO_2 structure, we constructed an extended Ti65O198 with hydrogen atoms to truncate the atomic dangling bonds on the support. Although the extended structure does not conform to the stoichiometry of TiO_2, it shows no convergence problems during the calculations. Fig. 4 indicates the stability of the Cu

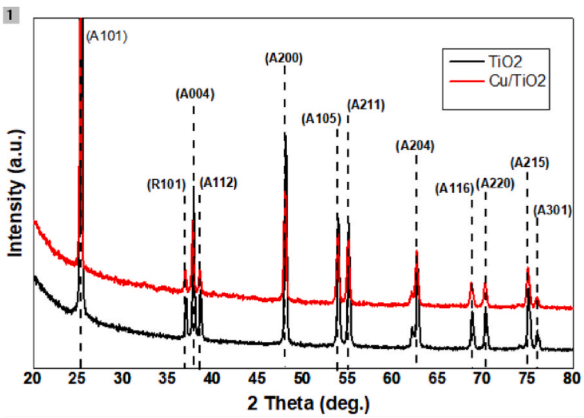

Fig. 2. XRD patterns of undoped TiO_2 and Cu/TiO_2.

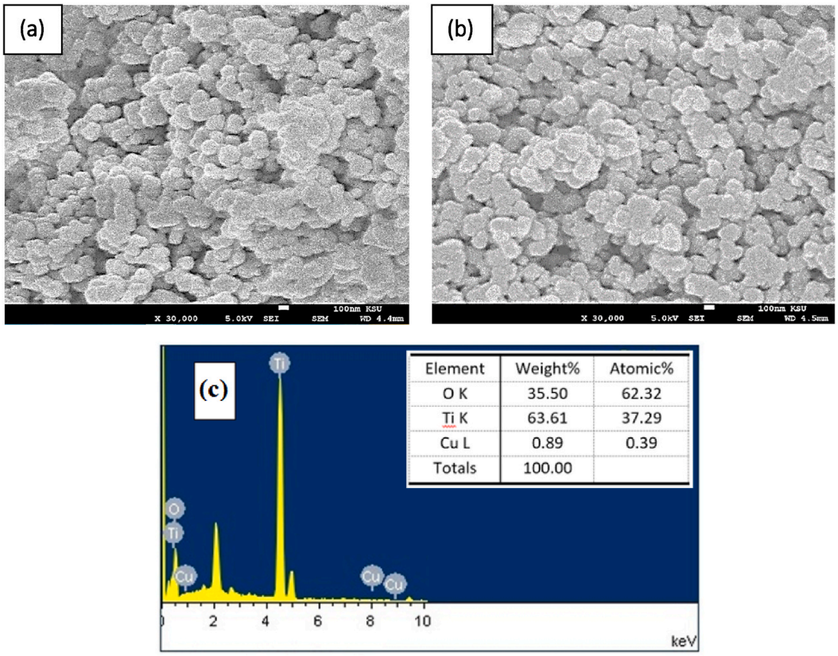

Fig. 3. Illustrates undoped TiO_2 (a), Cu-doped TiO_2 (b) in SEM images, and the EDS results for Cu-doped TiO_2.

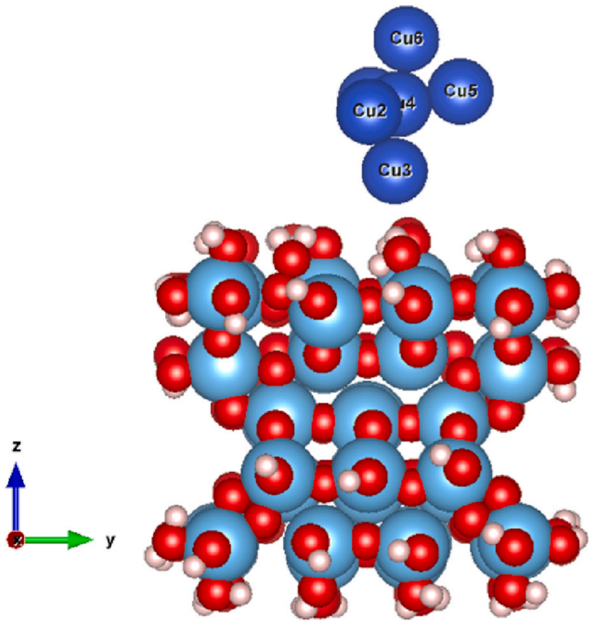

Fig. 4. The molecular dynamic calculation of the structure of Cu nanoparticle (blue balls) supported on TiO_2 structure (light blue and red balls) truncated by H atoms (grey balls). (For interpretation of the references to colour in this figure legend, the reader is referred to the Web version of this article.)

nanoparticle at the end of the 100 ps calculation in such a way that the nanoparticle atoms do not smear out away from the TiO_2 support. Since this calculation is meant for a qualitative study of the stability of the Cu nanoparticle on TiO_2 support, it is convenient to outline the calculation method here. We used the xtb software with the default GFN2-xTB parameterization method [26]. The calculation used the NVT ensemble at 298 K with a step size of 10 fs.

3.3. Dielectric properties

Dielectric research was conducted to explore the effect of Cu metal insertion on TiO_2 through the measurement of the complex impedance, Z^*. The real part of permittivity, ε' (or dielectric constant) and imaginary part of permittivity, ε'', were calculated by using Eq. 1, and 2 [27].

$$\varepsilon' = \frac{Z''}{\omega C_0 (Z'^2 + Z''^2)} \tag{1}$$

$$\varepsilon'' = \frac{Z'}{\omega C_0 (Z'^2 + Z''^2)} \tag{2}$$

Where C_0 is the vacuum capacitance, ω is the angular frequency, Z' and Z'' are the real and imaginary parts Z^*.

In Fig. 5, the dependence of ε' on the frequency at different temperatures (25, 50, 75, 100, and 120 °C) is illustrated for undoped TiO_2 (Fig. 5(a)) and Cu/TiO_2 (Fig. 5(b)). The same behaviors were observed for both undoped TiO_2 and Cu/TiO_2 in Fig. 5a and b. As the frequency decreased, the dielectric constant progressively rose, and as the frequency increased, the dielectric constant values reached a plateau. This behavior is normal and has also been observed by several investigators [28,29]. As the number of dipoles aligned in the direction of the applied electric field grows, the dielectric constant value increases due to the reduction of the frequency (f). However, at higher frequencies, the number of dipoles that follow the electric field oscillation decreases. Furthermore, the variation of ε' with frequency demonstrates the dispersion caused by Maxwell-Wagner type interfacial polarization at low frequencies. Cu/TiO_2 has a higher dielectric constant value compared to undoped TiO_2, possibly due to the presence of the transition metals which increase the charge carriers in the sample.

It is commonly known that the internal energy dissipation from the applied signal is indicated by the dielectric loss, $\varepsilon''/\varepsilon'$ [30]. The dielectric loss for undoped TiO_2 and Cu/TiO_2 as a function of frequency is displayed in Fig. 6(a) and (b). For Cu/TiO_2, the decrease in dielectric loss with increasing frequency [31] is probably related to the conductivity and/or interfacial polarization. Furthermore, an increase in the temperature results in decreased dielectric loss for both undoped TiO_2 and Cu/TiO_2.

3.4. AC conductivity

The real part of the conductivity, σ', was measured by using Eq. (3).

$$\sigma' = \frac{t}{A}\left[\frac{Z'}{Z'^2 + Z''^2}\right] = \varepsilon_0 \omega \varepsilon'' \tag{3}$$

where A is the surface area, t is the thickness, and ε_0 is the permittivity of free space. The frequency response of σ' is shown in Fig. 7(a) and (b) at different temperatures (25, 50, 75, 100, and 120 °C) for undoped TiO_2 and Cu/TiO_2. The conductivities of undoped TiO_2 and Cu-doped TiO_2 display a decreasing trend with temperature. Moreover, at low frequencies, undoped TiO_2 and Cu-doped TiO_2 show a plateau behavior, and σ' exhibits a frequency dependence at higher frequencies. This behavior is attributed to the increase in the ionic response to the field.

Fig. 8(a) and (b) illustrate the experimental data of Z' versus Z'' for undoped TiO_2 and Cu/TiO_2, respectively. The equivalent impedance circuit model used for fitting these experimental data is shown in Fig. 8(c), which includes a contact capacitor (Q1) in parallel with a polarization resistor (R1) and an R2-Q2 parallel resistor –capacitor circuit. The fitting procedure was performed via Z Simp Win Analyzer. Table 1 presents the data obtained from the fitting process. The ionic resistances of all samples increase with increasing temperature. Moreover, the impedance slightly decreased after modification with Cu (see Fig. 8(b) and Table 1).

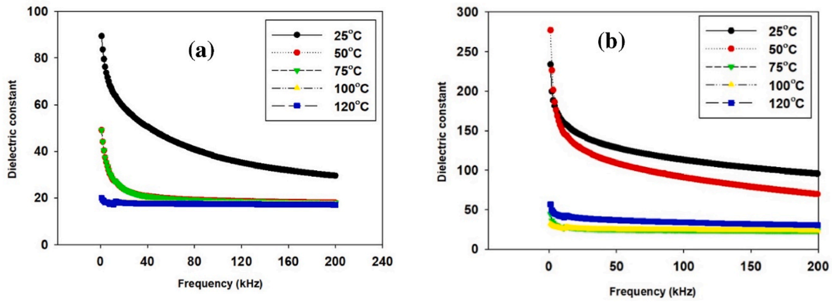

Fig. 5. Shows the dielectric constant for undoped TiO_2 (a) and Cu/TiO_2 (b) as a function of frequency at various temperatures.

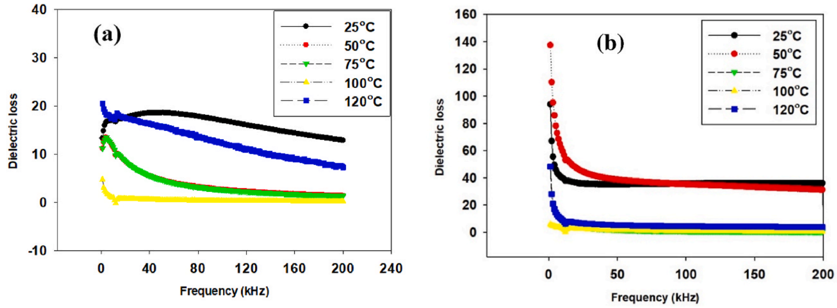

Fig. 6. Temperature-dependent dielectric loss for (a) undoped TiO_2 and (b) Cu/TiO_2 in relation to frequency.

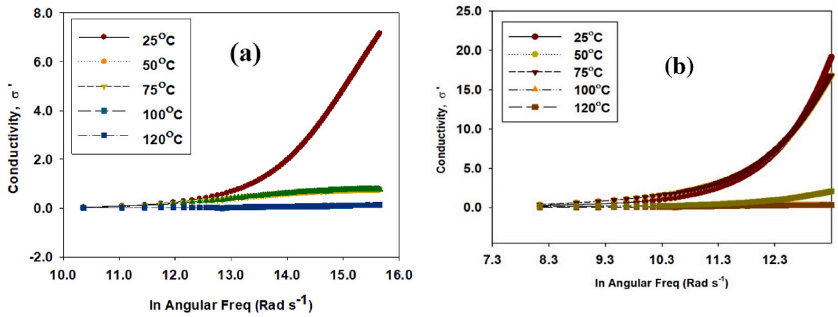

Fig. 7. Frequency dependence of conductivity at various temperatures for (a) undoped TiO_2 and (b) Cu-doped TiO_2.

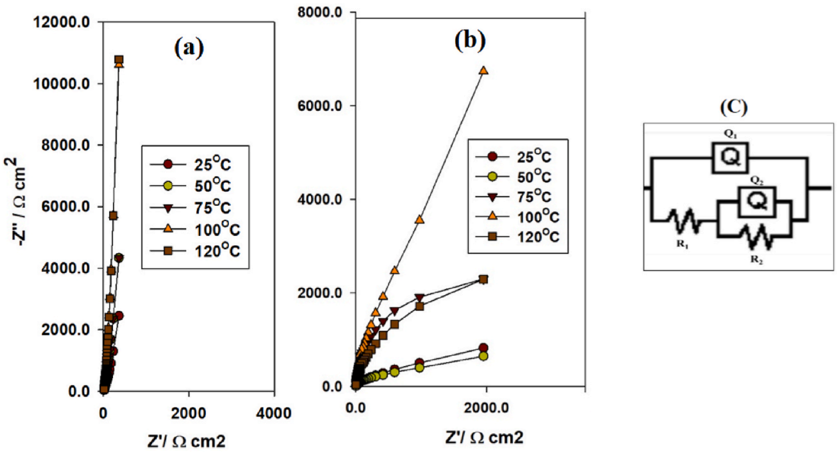

Fig. 8. Variation of d Z' with Z'' for (a) undoped TiO_2, (b) Cu/TiO_2, and (c) the equivalent circuit.

3.5. Optical properties of undoped TiO_2 and Cu-doped TiO_2

Fig. 9(a) shows how the absorption spectra for undoped TiO_2 and Cu/TiO_2 depend on wavelength and how adding Cu to TiO_2 increases absorption. Additionally, Fig. 9(b) demonstrates how the transmission spectra of undoped TiO_2 and Cu/TiO_2 vary depending on wavelength. For Cu/TiO_2 the transmittance increased with the wavelength, however for the undoped TiO_2 it decreases because of the different sample's crystallizations.

3.5.1. The energy gap

The energy band gap (Eg) was determined via the absorption coefficient from Eq. (4) [32]:

$$\alpha h = B\left(h - E_g\right)^n \tag{4}$$

n is an index that can be 1/2, 3/2, 2, or 3; h is the Planck constant; ν is the frequency of incoming light; and B is constant.

Table 1
The values of the fitting parameters for undoped TiO_2, and Cu/TiO_2.

Samples	Temperature (°C)	Q_1 (nF)	R_1 (MΩ)	Q_2 (nF)	R_2 (MΩ)
TiO_2	25	0.4377	0.0077	1423.9	1.952
	50	0.1272	1.1341	13.021	10.25
	75	0.8065	3.4550	24.66	100.5
	100	0.00182	290.57	54.661	325.12
	120	0.00212	964.5	3.0591	9745.2
Cu/TiO_2	25	270.9	0.2455	227.87	0.1571
	50	68.65	0.1599	273.81	0.587
	75	33.01	9.0434	72.312	0.5872
	100	61.934	13.422	27.61	1.1452
	120	0.0072	974.51	1.035	9745.6

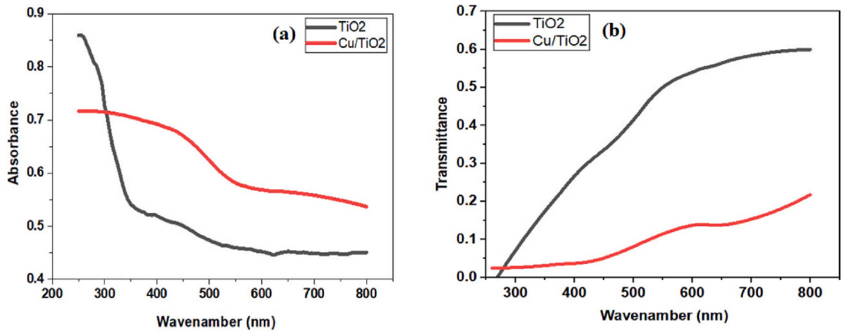

Fig. 9. The optical absorbance (a) and transmittance (b) spectra of undoped TiO_2 and Cu/TiO_2.

It was discovered that when $n = 2$, the best fit is obtained. The relationship between $(\alpha h\nu)^2$ and photon energy ($h\nu$) was used to compute the energy gap (Eg) of undoped TiO_2 and Cu/TiO_2, as illustrated in Fig. 10. The energy band was generated by extrapolating the straight-line portion of the energy axis $(h\nu)$ from Fig. 10 as revealed in Table 2. Lowering the value of E_g by Cu doping of TiO_2 may be related to oxygen vacancy deformation and the regularity of the anatase structure of TiO_2.

Additionally, variations in the energy gap might be linked to the quantum size effect brought about by the size variations in our nanoscale grains created by dopants. The reduced E_g of the Cu/TiO_2 combination allows for a variety of optical applications, including waveguides and light-emitting diodes.

3.5.2. The index of refraction

The refractive index has a major impact on the optical and material sciences. The transmittance and reflectance of materials may be assessed using ***UV***–vis spectrophotometer examination of the refractive index. The link between the transmittance T at normal incidence and the index of refraction n is illustrated by the Fresnel equations. The values of the refractive index were calculated using Eq. (5).

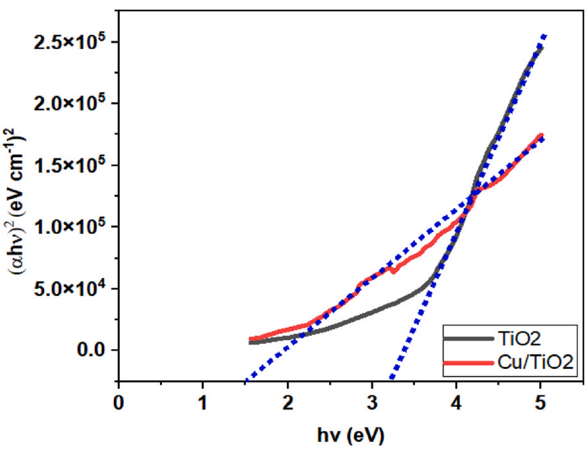

Fig. 10. The plotting of $(\alpha h\nu)^2$ with the energy photon $(h\nu)$ for undoped TiO_2 and Cu/TiO_2.

Table 2
Energy gap $\boldsymbol{E_g}$, energy of Urbach $\boldsymbol{E_U}$, steepness **S**, energy oscillation $\boldsymbol{E_o}$, energy dispersion $\boldsymbol{E_d}$, the index of refraction at wavelength infinity $\boldsymbol{n_\infty}$, and the fitting parameters $\boldsymbol{A}$ and $\boldsymbol{B}$ for undoped TiO_2 and Cu/TiO_2.

Samples	E_g (eV)	E_d (eV)	E_o (eV)	n_∞	A	B (μm^2)	E_U (eV)	S ($\times 10^{-2}$)
TiO_2	3.40	15.11	3.636	2.271	3.851	1.948	5.362	0.48
Cu/TiO_2	1.95	74.42	3.446	4.754	4.333	0.797	9.132	0.28

$$\boldsymbol{n} = \frac{\boldsymbol{2 - T + 2\sqrt{1 - T}}}{\boldsymbol{T}} \tag{5}$$

Fig. 11 illustrates the relationship between wavelength dispersion and refractive index for undoped TiO_2 and Cu/TiO_2. Using the best-fitting model, the values of n drop with increasing wavelength as Fig. 11 illustrates. The Cauchy dispersion relation was used to create the data in Fig. 11(a) [33]. The curve fitting of **n(λ)** yields Cauchy's coefficients **A** and **B**, by using **Eq. (6), as** illustrated in Table 2, where the dots are the values calculated from the transmission spectrum and the solid lines represent the curve fitting by using Cauchy dispersion relationship as in Fig. 11 (a).

$$\boldsymbol{n}(\lambda) = \boldsymbol{A} + \frac{\boldsymbol{B}}{\lambda^2} \tag{6}$$

The interior microstructure of the composite is altered during the synthesis process, giving this composite a high refractive index. Numerous optical applications for the higher refractive index in Cu/TiO_2 are possible [34,35].

To roughly validate the increase in the refractive index for Cu/TiO_2 compared to TiO_2, we have calculated the real refractive index for both materials using the default optical calculation settings in CASTEP software [36]. The calculation results are shown in Fig. 11 (b), where the refractive index for Cu/TiO_2 structure is effectively higher than that for TiO_2, agreeing with the general trend of the experimental data of Fig. 11(a). The calculations employed 48-atom supercells, $Ti_{16}O_{32}$ and $CuTi_{15}O_{32}$ having C2/c and I-4m2 space group symmetries, respectively, with common lattice parameters (a = b = 7.532410 Å, c = 11.076582 Å, α = β = 70.123°, and γ = 89.99°). The lattice parameters are common to both supercells because, for simplicity, $CuTi_{15}O_{32}$ was generated from the geometrically optimized $Ti_{16}O_{32}$ by substituting the Ti (at (0,0,0) site) by Cu. We emphasize that, for qualitative and preliminary calculations, we opted for the default settings in CASTEP. Systematic calculations will be deferred to future research.

3.5.3. Optical dispersion parameters

The single oscillator model provides the dispersion energy factor $\boldsymbol{(E_d)}$ and single oscillator energy $\boldsymbol{(E_o)}$**,** associated with the average intensity of the optical inter-band transition and the energy separation between the valence and conduction bands. These parameters are given by Wemple-DiDomenico via the following formula **(Eqs** [7,8,37].

$$\boldsymbol{n^2 = 1 + \frac{E_d E_o}{E_o^2 - (h\nu)^2}} \tag{7}$$

$$\boldsymbol{(n^2 - 1)^{-1} = \frac{E_o}{E_d} - \frac{(h\nu)^2}{E_d E_o}} \tag{8}$$

By plotting $(n^2 - 1)^{-1}$ with $(h\nu)^2$, **by using Eq. (8),** $\boldsymbol{E_o}$ and $\boldsymbol{E_d}$ are calculated from the slope and intercept of the linear fitting as shown in Fig. 12 and tabulated in Table 2.

By setting the wavelength in **Eq. (7)** to infinity owing to the electronic transformation, it is possible to compute the index of refraction at an infinite wavelength ($\boldsymbol{n_\infty}$) **as in Eqs.** [9,10]**:**

$$n_\infty^2 = 1 + \frac{E_d E_o}{E_o^2} \tag{9}$$

and then:

$$n_\infty = \sqrt{1 + \frac{E_d}{E_o}} \tag{10}$$

The values of E_o and E_d for TiO_2, Cu/TiO_2 were used to determine $\boldsymbol{n_\infty}$ **by using Eq. (10)** and listed in Table 2.

3.5.4. Urbach energy and steepness parameter

The Urbach edge, sometimes called the absorption edge, is characterized by a photon energy-dependent exponential rise in the absorption coefficient. The exponential tail size of the absorbance edge may be determined via Urbach energy $\boldsymbol{(E_U)}$. The Urbach energy represents the band tail width of the localized states, and the experimental relationship yields the following data for the exponential absorption tails as **in Eq. (11)** [38]:

$$\boldsymbol{\alpha = \alpha_o e^{\left(\frac{h\nu}{E_U}\right)}} \tag{11}$$

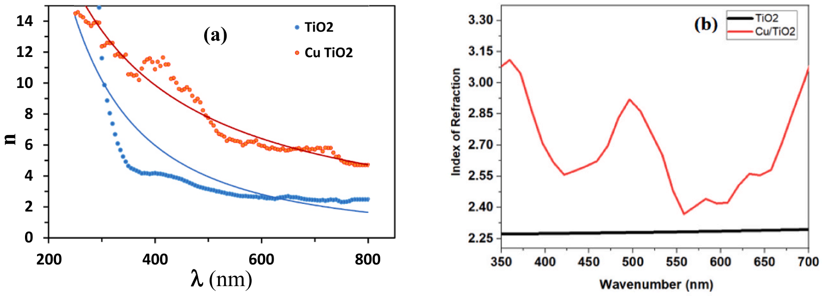

Fig. 11. (a) The refractive index dispersion with wavelengths for undoped TiO_2 and Cu-doped TiO_2. (b) Calculated real refractive index using the time dependent density functional theory.

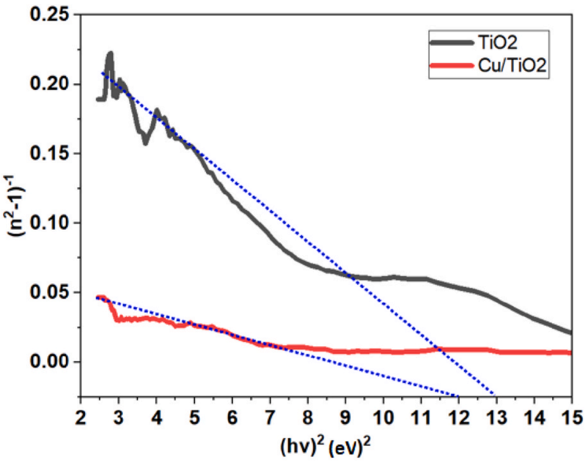

Fig. 12. The relation of $(n^2\text{-}1)^{-1}$ versus $(h\nu)^2$ for undoped TiO_2 and Cu/TiO_2.

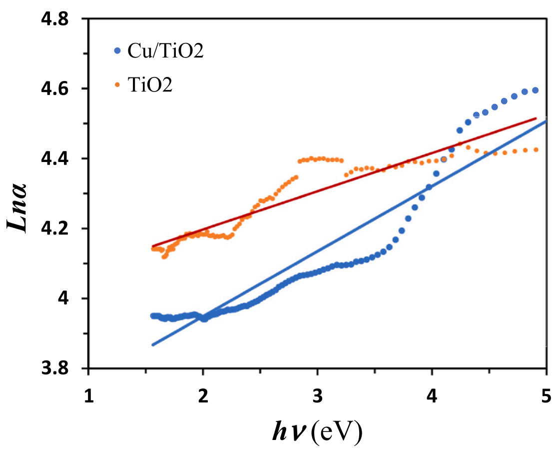

Fig. 13. The relation between ***Lnα*** and the photon energy (***hν***) for the samples.

$$\ln \alpha = \ln \alpha_o + \frac{h\nu}{E_U} \tag{12}$$

In which α_o is a constant. Visualizing the correlation between **($ln\alpha$)** and photon energy **($h\nu$)**, as shown in Fig. 13 and in Table 2, allows the use **of Eq. (12)** to determine the Urbach energy for the samples that were utilized.

A higher density of defect states in the Cu-doped TiO_2 film may be the cause of the observed increase in E_U with Cu doping [39,40]. At room temperature (T = 300 K), the steepness parameter S may be calculated as follows [41]:

$$S = \frac{K_B T}{E_U} \tag{13}$$

The steepness parameter $\boldsymbol{S}$ can be calculated by knowing the Urbach energy **(E_U)** from **Eq. (13)** as in Table 2 for TiO_2 and Cu/TiO_2, where K_B is the Boltzmann constant.

4. Conclusion

Employing an accessible and efficient incipient wet impregnation approach, we successfully synthesized Cu-doped TiO_2. X-ray diffraction was utilized to analyze the resulting Cu/TiO_2. The anatase phase and traces of the rutile phase were effectively produced, as evidenced by the positions of the X-ray peaks according to the X-ray diffraction patterns.

The structural stability of Cu/TiO_2 was qualitatively validated through semi-empirical molecular dynamic calculations. In comparison to undoped TiO_2, Cu/TiO_2 exhibits a higher dielectric constant. However, with an increase in temperature, both undoped TiO_2 and the Cu/TiO_2 demonstrate a reduction in conductivity. Additionally, at low frequencies, both undoped TiO_2 and Cu/TiO_2 exhibit a plateau behavior in the conductivity profile; however, at higher frequencies, they display a frequency-dependent behavior. The optical absorbance and transmittance of the TiO_2 material are influenced by the introduction of Cu particles. Cu was blended with TiO_2 to reduce the energy band gap value, making it suitable for various optical applications, including optoelectronic devices. Optical dispersion properties at high wavelengths, such as dispersion energy, oscillation energy, and refractive index, were calculated. Furthermore, owing to internal structural changes and crystallinity, the refractive index values for the Cu/TiO_2 material significantly increased. This was further validated by density functional calculation of the optical properties of undoped TiO_2 and Cu/TiO_2 in the optical range.

Author contributions

Hana Al-Refai: Writing – review & editing, Writing – original draft, Investigation, Formal analysis, Data curation. Ali Bashal: Writing – review & editing, Writing – original draft, Visualization, Validation, Resources, Methodology, Conceptualization. R. M. Ibrahim: Writing – original draft, Software, Investigation, Formal analysis. Ayman A. Zaki: Writing – review & editing, Writing – original draft, Visualization, Validation, Methodology, Investigation, Formal analysis, Data curation

Declaration of competing interest

The authors declare the following financial interests/personal relationships which may be considered as potential competing interests:Ali H. Bashal reports financial support was provided by Taibah University. Ali H. Bashal reports a relationship with Taibah University that includes: employment. No other activity If there are other authors, they declare that they have no known competing financial interests or personal relationships that could have appeared to influence the work reported in this paper.

References

[1] D.J. Ahirrao, H.M. Wilson, N. Jha, TiO2-nanoflowers as flexible electrode for high performance supercapacitor, Appl. Surf. Sci. 491 (2019) 765–778, https://doi.org/10.1016/j.apsusc.2019.05.076.

[2] E.P. Da Silva, A.F. Rubira, O.P. Ferreira, R. Silva, E.C. Muniz, In situ growth of manganese oxide nanosheets over titanium dioxide nanofibers and their performance as active material for supercapacitor, J. Colloid Interface Sci. 555 (2019) 373–382, https://doi.org/10.1016/j.jcis.2019.07.064.

[3] P. Pascariu, M. Homocianu, L. Vacareanu, M. Asandulesa, Multi-functional materials based on Cu-doped TiO2 ceramic fibers with enhanced pseudocapacitive performances and their dielectric characteristics, Polymers 14 (21) (2022) 4739, https://doi.org/10.3390/polym14214739.

[4] I. Heng, C.W. Lai, J.C. Juan, A. Numan, J. Iqbal, E.Y.L. Teo, Low-temperature synthesis of TIO2 nanocrystals for high performance electrochemical supercapacitors, Ceram. Int. 45 (4) (2019) 4990–5000, https://doi.org/10.1016/j.ceramint.2018.11.199.

[5] Z. Zhang, F. Xiao, Y. Guo, S. Wang, Y. Liu, One-pot self-assembled three-dimensional TiO2-graphene hydrogel with improved adsorption capacities and photocatalytic and electrochemical activities, ACS Appl. Mater. Interfaces 5 (6) (2013) 2227–2233, https://doi.org/10.1021/am303299r.

[6] C. Guan, X. Xia, N. Meng, Z. Zeng, X. Cao, C. Soci, et al., Hollow core–shell nanostructure supercapacitor electrodes: gap matters, Energy Environ. Sci. 5 (10) (2012) 9085–9090, https://doi.org/10.1039/C2EE22815G.

[7] M. Dhonde, K. Sahu, V. Murty, S.S. Nemala, P. Bhargava, S. Mallick, Enhanced photovoltaic performance of a dye sensitized solar cell with Cu/N Co-doped TiO 2 nanoparticles, J. Mater. Sci. Mater. Electron. 29 (2018) 6274–6282, https://doi.org/10.1007/s10854-018-8605-3.

[8] H. Wang, Z. Tang, L. Sun, Y. He, Y. Wu, Z. Li, Capacitance performance enhancement of TiO 2 doped with Ni and graphite, Rare Met. 28 (2009) 231–236, https://doi.org/10.1007/s12598-009-0045-z.

[9] X. Ning, X. Wang, X. Yu, J. Zhao, M. Wang, H. Li, et al., Outstanding supercapacitive properties of Mn-doped TiO2 micro/nanostructure porous film prepared by anodization method, Sci. Rep. 6 (1) (2016) 22634, https://doi.org/10.1038/srep22634.

[10] Y. Qian, J. Du, D.J. Kang, Enhanced electrochemical performance of porous Co-doped TiO2 nanomaterials prepared by a solvothermal method, Microporous Mesoporous Mater. 273 (2019) 148–155, https://doi.org/10.1016/j.micromeso.2018.06.056.

[11] G.B. Soares, R.A.P. Ribeiro, S.R. De Lazaro, C. Ribeiro, Photoelectrochemical and theoretical investigation of the photocatalytic activity of TiO 2: N, RSC Adv. 6 (92) (2016) 89687–89698, https://doi.org/10.1039/C6RA15825K.
[12] A. Gupta, K. Sahu, M. Dhonde, V. Murty, Novel synergistic combination of Cu/S co-doped TiO2 nanoparticles incorporated as photoanode in dye sensitized solar cell, Sol. Energy 203 (2020) 296–303, https://doi.org/10.1016/j.solener.2020.04.043.
[13] S.G. Krishnan, P. Archana, B. Vidyadharan, Misnon II, B.L. Vijayan, V.M. Nair, et al., Modification of capacitive charge storage of TiO2 with nickel doping, J. Alloys Compd. 684 (2016) 328–334, https://doi.org/10.1016/j.jallcom.2016.05.183.
[14] A. Tyagi, N. Singh, Y. Sharma, R.K. Gupta, Improved supercapacitive performance in electrospun TiO2 nanofibers through Ta-doping for electrochemical capacitor applications, Catal. Today 325 (2019) 33–40, https://doi.org/10.1016/j.cattod.2018.06.026.
[15] C. Vidyasagar, Y.A. Naik, T. Venkatesha, P. Manjunatha, Sol–gel synthesis using glacial acetic acid and optical properties of anatase Cu–TiO2 nanoparticles, Journal of Nanoengineering and Nanomanufacturing 2 (1) (2012) 91–98, https://doi.org/10.1166/jnan.2012.1058.
[16] V. Krishnakumar, S. Boobas, J. Jayaprakash, M. Rajaboopathi, B. Han, M. Louhi-Kultanen, Effect of Cu doping on TiO 2 nanoparticles and its photocatalytic activity under visible light, J. Mater. Sci. Mater. Electron. 27 (2016) 7438–7447, https://doi.org/10.1007/s10854-016-4720-1.
[17] M. Dhonde, K. Sahu Dhonde, K. Purohit, V.V.S. Murty, Facile synthesis of Cu/N co-doped TiO2 nanoparticles and their optical and electrical properties, Indian J. Phys. 93 (1) (2019) 27–32, https://doi.org/10.1007/s12648-018-1275-4.
[18] Mahesh Dhonde, Kirti Sahu, V.V.S. Murty, Cu-doped TiO2 nanoparticles/graphene composites for efficient dye-sensitized solar cells, Sol. Energy 220 (2021) 418–424, https://doi.org/10.1016/j.solener.2021.03.072.
[19] Mahesh Dhonde, Kirti Sahu, V.V.S. Murty, Siva Sankar Nemala, Parag Bhargava, Surface plasmon resonance effect of Cu nanoparticles in a dye sensitized solar cell, Electrochim. Acta 249 (2017) 89–95, https://doi.org/10.1016/j.electacta.2017.07.187.
[20] Kirti Sahu, Mahesh Dhonde, Vemparala Venkata Satyanarayana Murty, Microwave-assisted hydrothermal synthesis of Cu-doped TiO2 nanoparticles for efficient dye-sensitized solar cell with improved open-circuit voltage, Int. J. Energy Res. 45 (4) (2021) 5423–5432, https://doi.org/10.1002/er.6169.
[21] Shuang Shu, Hongjun Wang, Xinyan Guo, Yan Wang, Xiaolan Zeng, Efficient photocatalytic degradation of sulfamethazine by Cu-CuxO/TiO2 composites: performance, photocatalytic mechanism and degradation pathways, Sep. Purif. Technol. 323 (2023) 124458, https://doi.org/10.1016/j.seppur.2023.124458.
[22] Petronela Pascariu, Mihaela Homocianu, Loredana Vacareanu, Mihai Asandulesa, Multi-functional materials based on Cu-doped TiO2 ceramic fibers with enhanced pseudocapacitive performances and their dielectric characteristics, Polymers 14 (21) (2022) 4739, https://doi.org/10.3390/polym14214739.
[23] A.H. Bashal, M.H. Saad, M.A. Khalafalla, The effect of nickel percentage on the dielectric properties of bentonite, J. Taibah Univ. Sci. 14 (1) (2020) 496–499, https://doi.org/10.1080/16583655.2020.1747216.
[24] K.P. Wang, H. Teng, Zinc-doping in TiO 2 films to enhance electron transport in dye-sensitized solar cells under low-intensity illumination, Phys. Chem. Chem. Phys. 11 (41) (2009) 9489–9496, https://doi.org/10.1039/B912672D.
[25] S. Mofokeng, V. Kumar, R. Kroon, O. Ntwaeaborwa, Structure and optical properties of Dy3+ activated sol-gel ZnO-TiO2 nanocomposites, J. Alloys Compd. 711 (2017) 121–131, https://doi.org/10.1016/j.jallcom.2017.03.345.
[26] C. Bannwarth, S. Ehlert, S. Grimme, GFN2-xTB—an accurate and broadly parametrized self-consistent tight-binding quantum chemical method with multipole electrostatics and density-dependent dispersion contributions, J. Chem. Theor. Comput. 15 (3) (2019) 1652–1671, https://doi.org/10.1021/acs.jctc.8b01176.
[27] R. Khalil, Impedance and modulus spectroscopy of poly (vinyl alcohol)-Mg [ClO4] 2 salt hybrid films, Appl. Phys. A 123 (6) (2017) 422, https://doi.org/10.1007/s00339-017-1026-y.
[28] A.H. Bashal, M. Khalafalla, T. Abdel-Basset, Dielectric properties and AC conductivity of chitosan-La 2 O 3 nanocomposite, Arabian J. Sci. Eng. 46 (2021) 5859–5864, https://doi.org/10.1007/s13369-020-04958-w.
[29] O.A. Desouky, The effect of SiO 2 addition on dielectric properties and microstructure of ZnNiO 2: based ceramics, SN Appl. Sci. 2 (2020) 1–16, https://doi.org/10.1007/s42452-019-1891-4.
[30] A. Singh, S. Narang, K. Singh, P. Sharma, O. Pandey, Structural, AC conductivity and dielectric properties of Sr-La hexaferrite, Eur. Phys. J. Appl. Phys. 33 (3) (2006) 189–193, https://doi.org/10.1051/epjap:2006016.
[31] P. Liu, V.M.H. Ng, Z. Yao, J. Zhou, Y. Lei, Z. Yang, et al., Facile synthesis and hierarchical assembly of flowerlike NiO structures with enhanced dielectric and microwave absorption properties, ACS Appl. Mater. Interfaces 9 (19) (2017) 16404–16416, https://doi.org/10.1021/acsami.7b02597.
[32] K. Hemalatha, G. Sriprakash, M. Ambika Prasad, R. Damle, K. Rukmani, Temperature dependent dielectric and conductivity studies of polyvinyl alcohol-ZnO nanocomposite films by impedance spectroscopy, J. Appl. Phys. 118 (15) (2015), https://doi.org/10.1063/1.4933286.
[33] A.A. Zaki, A.A. El-Amin, Effect of cell thickness on the electrical and optical properties of thin film silicon solar cell, Opt. Laser Technol. 97 (2017) 71–76.
[34] O.G. Abdullah, S.B. Aziz, K.M. Omer, Y.M. Salih, Reducing the optical band gap of polyvinyl alcohol (PVA) based nanocomposite, J. Mater. Sci. Mater. Electron. 26 (2015) 5303–5309, https://doi.org/10.1007/s10854-015-3067-3.
[35] T.G. Urs, G. Gowtham, M. Nandaprakash, D. Mahadevaiah, Y. Sangappa, R. Somashekar, Determination of force constant and refractive index of a semiconducting polymer composite using UV/visible spectroscopy: a new approach, Indian J. Phys. 91 (2017) 53–56, https://doi.org/10.1007/s12648-016-0905-y.
[36] S.J. Clark, M.D. Segall, C.J. Pickard, P.J. Hasnip, M.I. Probert, K. Refson, et al., First principles methods using CASTEP, Z. für Kristallogr. - Cryst. Mater. 220 (5–6) (2005) 567–570, https://doi.org/10.1524/zkri.220.5.567.65075.
[37] A.A. Zaki, M. Khalafalla, K.H. Alharbi, K.D. Khalil, Synthesis, characterization and optical properties of chitosan–La2O3 nanocomposite, Bull. Mater. Sci. 45 (2022) 128.
[38] A.Z. Ayman, A.R. Hanaa, H.B. Ali, A.H.K. Mohammed, Tailoring optical and dielectric properties of TiO2 through mono- and Co-doping with Ag and Sr, J. Phys. Chem. Solid. 27 (2023) 11809, https://doi.org/10.1016/j.jpcs.2023.111809.
[39] N. Banu, A.H. Bhuiyan, K.S. Hossain, Characterization of structural and optical properties of plasma polymerized diethanolamine thin films, Adv. Polym. Technol. 37 (8) (2018) 3084–3094, https://doi.org/10.1002/adv.22079.
[40] S. Fayek, M. Balboul, K. Marzouk, Optical, electrical, and thermal studies on (As2Se3) 3- x (As2Te3) x glasses, Thin Solid Films 515 (18) (2007) 7281–7285, https://doi.org/10.1016/j.tsf.2007.03.039.
[41] A.Z. Ayman, T.A. Abdel-Basset, H. Mohammed, H. Ali, Dielectric and optical properties of chitosan-Pb and chitosan-Bi nanocomposites, J. Mater. Sci. Mater. Electron. 32 (2021) 3603–3611.